Spring 5-7-2020

Ultrasound-Assisted Post-Pyrolysis Magnetization of Microporous Biochar for Effective Removal of Heavy Metals

Ronish Shrestha

Ultrasound-Assisted Post-Pyrolysis Magnetization of Microporous Biochar for Effective Removal of Heavy Metals

by
Ronish Man Shrestha

A thesis submitted to the faculty of The University of Mississippi in partial fulfillment of the requirements of the Sally McDonnell Barksdale Honors College.

Oxford
May 2020

Approved By

Advisor: Dr. Baharak Sajjadi

2nd Reader: Dr. Wei-Yin Chen

3rd Reader: Dr. John O' Haver

4th Reader: Dr. Sasan Nouranian

ABSTRACT

Low cost and efficient adsorption of heavy metals from wastewater and thorough removal of adsorbent after water treatment have become the two essential needs for the commercial use of any adsorbent. Biochar (BC), the solid byproduct of pyrolysis with microporous carbonaceous structure, has been increasingly recognized as an efficient adsorbent for a vast number of pollutants. Magnetization, though eases the separation and reuse of BC, significantly reduces its adsorption capacity to a comparatively much higher extent. In this study, a hybrid post-pyrolysis magnetization was developed which sustained and even significantly increased the adsorption capacity of biochar. The process included i) structural modification of biochar under ultrasound waves, ii) magnetization with magnetite (Fe_3O_4) nanoparticles and iii) functionalization with 3-aminopropyl triethoxysilane. Ultrasound irradiation exfoliates and breaks apart the irregular graphite layers of biochar, and creates new/opens the blocked microspores, thus enhancing the BC's porosity. On the other hand, 3-aminopropyl triethoxysilane stabilizes the magnetic nanoparticles on the biochar surface, while it participates in water treatment through the strong chelation ability of its amino groups toward metal ions. Scanning electron microscope image demonstrated the stable and uniform distribution of Fe_3O_4 nanoparticles on the surface of microporous biochar and Fourier-transform infrared spectroscopy suggested effective surface functionalization. In addition, although magnetization usually reduces the porosity of carbonaceous adsorbents, acoustic activation prior to magnetization increased the microporosity of biochar (from 123 for Raw-BC to 155 m^2/g for acoustic-based magnetic biochar). Preliminary results of Ultraviolet–visible spectroscopy showed that acoustic-based magnetic biochar exhibited a much greater ability to remove Ni and Pb, with 139% and 38% higher adsorption compared to raw biochar. Almost complete removal of Pb (91%) was observed by magnetic-BC.

TABLE OF CONTENTS

LIST OF TABLES AND FIGURES

LIST OF ABBREVIATIONS

US – Ultrasound

BC – Biochar

TES - 3-aminopropyl triethoxysilane

Fe-NP – Fe_3O_4 nanoparticles

SEM – Scanning Electron microscope

FTIR – Fourier Transform Infrared Spectroscopy

BET - BrunauereEmmetteTeller

1 Introduction

Owing to the rapid boom in industrialization, the proper treatment of the heavy metals from industrial wastewater has become of monumental importance [1]. Heavy metals are readily soluble in aquatic environs and once these connect up to food or drinking water chain, considerable concentrations can accumulate inside the human body which can be lethal if allowed to go beyond tolerable limits [2, 3]. Nickel and Lead, which are used in manufacturing processes of batteries, super-alloys, and smelting of sulfide ores, are considered to be severely toxic even at low concentrations. Biosorbents and activated carbon are good adsorbents for these heavy metals but compared to biochar, are relatively expensive. Thus, for cost-effective interests, a wide variety of biochars have been extensively studied for their ability to sorb heavy metals [4-6]. Most derived biochars contribute to heavy metal adsorption through the processes of cation release, functional groups complexations and other physical and surface interactions. These, in turn, include mechanisms such as co-precipitation where a heavy metal cation substitutes another cation on the biochar's surface. The heavy metal cations can also be directly adsorbed into the pores on the biochar through physical adsorption and surface precipitation (amorphous) [7].

A hindrance to these ongoing advancements in heavy metal adsorption has been biochar recovery after wastewater treatment. Time-consuming steps like centrifugation and filtration are unlikely to be efficient in large scale applications. So, the magnetization of biochar has provided a novel approach, allowing practical use of small particle size adsorbents which have high surface areas and fast adsorption kinetics. With the use of a magnet, magnetic biochar can be easily and quickly separated after adsorbing heavy metal contaminants from water. This makes either of batch and stirred processes a viable option while also overcoming the drawbacks caused by filtration of small particle size adsorbents and delivering faster adsorption kinetics [8].

Impregnation, co-precipitation, and liquid reduction are the most common methods have been used to prepare magnetic biochar. Impregnation includes mixing the biomass with a ferric or ferrous chloride precursor solution, and subsequent pyrolysis of the obtained biomass in an inert environment under high temperature. This single-step pyrolysis of $FeCl_3$ loaded biomass can produce the biochar with magnetic properties but simultaneously produces secondary pollution, is costly and may not address any desired functional group on biochar surface [9]. Surface functional groups which support adsorption through complexation become limited via this process as they react with iron in various oxidation reactions during pyrolysis, reducing biochar's heavy metal adsorption capacity significantly [10, 11]. The magnetization of biochar has typically been achieved through the traditional method of chemical co-precipitation with magnetite (Fe_3O_4) [10, 12]. In this process, iron oxides of magnetic nature are precipitated directly onto the biochar with the use of biocarbon and a mixed Fe^{2+}/Fe^{3+} salt solution. These iron compounds have been used individually or in unison to impart magnetism on the biochar [13, 14]. The liquid-phase reduction method comprises mixing the biocarbon with Fe^{2+} salt solution and then reducing Fe^{2+} to the zero-valent iron on biochar surface using a reducing agent ($NaBH_4/KBH_4$). The two latter methods method can reduce the porosity of biochar due to the aggregation of iron oxides in the aqueous solution. This results in a decrease in the surface area and hence the adsorption capability of biochar [15]. Even with the optimum amount of doping, the decrease in heavy metal adsorption is prevalent. To reap the benefits of magnetic separation, overcoming these drawbacks is crucial [16].

Ultrasound irradiation has been recently introduced as an effective method for activation of carbonaceous compounds with graphitic structures. Ultrasonic irradiation with a frequency between 20 kHz and 1 MHz generates microscopic cavitation which is defined as the sequential formation-generation, growth, and collapse of microbubbles [17]. Generation of micro-jets, shock waves and

highly pressurized over-heated regions known as hot-spots are the most well-known implications of explosion of micro-bubbles (cavitation phenomenon). [17]. The hot spots, with the temperature of 5000 °C, pressure of 1000 atm and heating-cooling rates above 10^{10} K/s, hold sufficient energy to activate or split the larger particles into smaller ones, clean smooth surfaces, and increase the porosity of solid surfaces [18, 19]. The effect of ultrasound on graphite oxide was first discovered by Stanokovich, who found that a mild ultrasonic treatment (F=80 kHz, 150 W) of graphite oxides for 1 hour exfoliates its layers and forms stable aqueous dispersions that consist almost entirely 1-nm thick sheets [20]. The physical structure of biochar comprises clusters of parallel graphene oxide layers consisting of acquirable oxygen functional groups [21-23]. Given this fact and inspired by Stanokovich's works, our group investigated the interaction of ultrasound/biochar/CO_2/water and discovered remarkable synergisms upon treating biochar (BC) with ultrasound (US) irradiation, which include disarrangement & exfoliation of BC's graphitic structure, mineral leaching & significant increase in BC's porosity, significant increase in BC's internal surface area, creation of new and opening of blocked mesopores, enhanced carbon and hydrogen content of biochar [24]. We further expanded the application of this advanced activation process to develop an effective adsorbent for removal of pollutant from either water or air.

As a sequel to our previous works, this study proposes an acoustic based magnetization process which not only facilitate biochar removal after adsorption but also increases its adsorption capacity. The process includes three distinct steps I) physical activation of biochar under ultrasound irradiation (USBC), II) magnetization of sono-activated biochar with Fe_3O_4 nanoparticles (USMBC) and III) functionalization of USMBC with 3-(Triethoxysilyl)propylamine (TES) to improve the stability of Fe_3O_4 nanoparticles (Fe-NP) on the biochar surface and increase adsorption sites for heavy metals.

2 Materials and methods

2.1 Materials

Commercial Pinewood biochar supplied by Biochar Now (Berthoud Colorado, U.S.A) was used for the purpose of this experiment. The biomass is pyrolyzed at a temperature between 550 and 600^{o}C in a kiln reactor with multi-zone combustion chamber, after which nitrogen is introduced to discontinue the process. The reagents used in the magnetization process were Iron(III) Chloride ($FeCl_3$, 97% purity), Iron(II) Sulfate Heptahydrate ($FeSO_4.7H_2O$, 99.0% purity), 3-(Triethoxysilyl)propylamine (TES) and Ammonium Hydroxide (NH_4OH, 28% NH_3 in H_2O, 99.0%), all of which were obtained from Sigma Aldrich. The chemicals for preparing stock heavy metal solutions, Lead (II) Chloride (98% purity) and Nickel (II) Chloride (98% purity), were also obtained from Sigma Aldrich. The standards used for the measuring heavy metal concentration, TNT856 for Nickel and TNT850 for Lead, were purchased from Hach.

2.2 Experimental Method

2.2.1 Ultrasound Treatment of biochar and magnetization

The raw biochar was first ground in a ball mill grinder and sieved several times to the range of 75-125µm. To modify the physical structure, a mixture of biochar in water of a specific ratio was irradiated with low-frequency ultrasound (QSonica sonicator model No. Q700, max power 700W). The duration of ultrasound treatment was selected based on the optimum values (30 and 60s) obtained from our previous studies [21, 23]. Fe-NPs were produced separately. Iron (III) Chloride ($FeCl_3$) and Iron (II) Sulfate Heptahydrate ($FeSO_4.7H_2O$) with a 2:1 weight ratio were dissolved in pre-degassed distilled water. The solution was stirred for 30min at room temperature. NH_4OH 28% was then added to precipitate the Iron(III) Oxide (Fe_3O_4) nanoparticles and the mixture was kept

stirring for 5hrs at 80°C. All these syntheses were performed in an inert atmosphere (N_2) to avoid uncontrolled oxidation and formation of non-magnetic oxides through oxidation of Fe^{2+} to Fe^{3+}, giving higher yeild of magnetite particles. The black precipitate was collected by filtration; washed and dried at 60°C for 12h. In the next step, varying ratios of ultrasono-activated biochar (US-BC) and Iron(III) Oxide nanoparticles (1:1, 2:1, and 3:1) were mixed with distilled water and stirred for 2hrs at 50°C to obtain Fe_3O_4-loaded biochar. The ultrasono-magnetized biochar was then subjected to chemical functionalization with 3-aminopropyl triethoxysilane (TES). The dried composite of Fe_3O_4-loaded biochar was added to the diluted solutions of TES in water (5, 10 and 15mL in distilled water) and stirred for 8h at 50°C. Eventually, the functionalized-magnetized biochar was filtered, washed with distilled water several times (until pH is closed to 7) and dried at 60°C for 12h, Figure 1. The synergisms of Fe_3O_4 loading, TES functionalization, and ultrasound activation were investigated with respect to adsorption rates of Nickel and Lead.

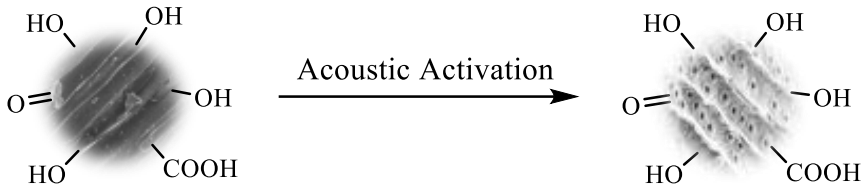

$$2Fe^{3+} + Fe^{2+} \xrightarrow{8OH^-} 2Fe(OH)_3 + Fe(OH)_2 \longrightarrow Fe_3O_4 + 4H_2O$$

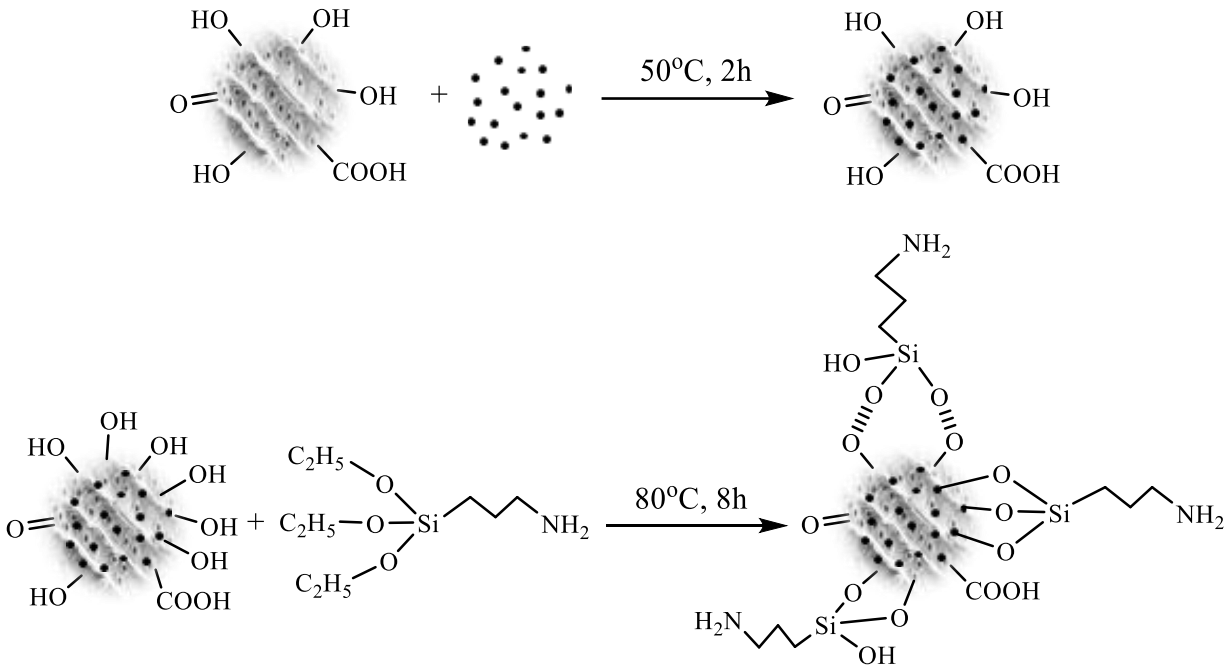

Figure 1. Biochar magnetization process and the mechanism of TES functionalization, developed partially based on [25, 26]

2.3 Characterizations of the Adsorbent

The porosity and surface area of the raw, ultra-sonicated, and magnetized biochars were measured using a surface area analyzer (3Flex Series, Micromeritics). The morphological analysis was also conducted using SEM (JSM-7200 Scanning Electron Microscope, JEOL USA Inc., Thad Cochran Research Center, MS) to study the structural surface of synthesized biochars. The presence of iron and organic compounds (C, N, H, O) were investigated through combustion analysis by Huffman Hazen Laboratory, Colorado, USA Fourier. Raman (LabRam HR Evolution) and Transform Infrared (FTIR, Cary 660 FTIR Agilent) spectroscopies were also employed to characterize the graphitic structure of samples and surface functional groups, the doping of iron oxides on the biochar surface and the presence of TES.

2.4 Nickel and Lead Adsorption Studies

Distinct solutions containing 100 mg/L Ni^{2+} and Pb^{2+} were prepared using powder Nickel (II) Chloride (98%, Sigma Aldrich) and powder Lead (II) Chloride (98%, Sigma Aldrich), respectively. In each adsorption experiment, 0.5g of the synthesized biochar was added to a 50mL solution of 100 mg/L Ni^{2+} or Pb^{2+} and was stirred in a shaker for varying durations (30min, 1, 2, 4, and 6h), after which the biochar was separated from the solution using strong neodymium magnets and further by filtration. The metal ion concentration of the filtrate was determined through UV-VIS spectroscopy (DR6000, Hach) using the respective standard kits (TNT856 For nickel and TNT850 for lead).

2.5 Initial Challenges

Before moving onto the topic of magnetization, a well-suited biochar had to be chosen with appropriate amount of adsorption capacity for Nickel and Lead metal ions. Deciding on the biochar source was pretty simple since the lab already had ample amount of commercial pinewood biochar. The problem was deciding on the biochar's particle size range. Based on previous literature, smaller particle sizes have better adsorption, but only up to a certain point. So, I had to grind and sieve biochar of different size ranges and run adsorption tests on all of them before coming up with the optimum range.

Starting the magnetization of biochar was another hurdle since this was a very new subject for our lab. Initially, we decided on precipitating iron oxides directly onto the biochar, which ended up significantly reducing the adsorption capacity of the biochar towards Lead and especially Nickel ions. In fact, we were not seeing any noticeable adsorption for Nickel. After discussing, we concluded that the biochar was getting oversaturated with iron oxides which were covering up the pores or adsorption sites on the biochar surface. So, we came up with a process of firstly precipitating iron oxides separately, drying them, and then mixing it with biochar in a distilled water solution.

This increased the preparation time for our magnetized biochar but significantly helped in sustaining the adsorption capability.

3 Results and Discussion

3.1 Mechanism of Chemical Activation of Biochar

The co-precipitation process has a well-known mechanism as represented by Eq. (1-3). This process can synthesize the particle size in the range above 10 nm.

$$Fe^{2+} + 2OH^{-} \rightarrow Fe(OH)_2 \quad (1)$$

$$Fe^{3+} + 3OH^{-} \rightarrow Fe(OH)_3 \quad (2)$$

$$Fe(OH)_2 + 2Fe(OH)_3 \rightarrow Fe_3O_4 + 4H_2O \quad (3)$$

Though loading the magnetic Fe_3O_4 on the surface, deliver magnetization property to the biochar matrix, some magnetic nanoparticles may be detached when the biochar comes in contact with aqueous solutions. The main objectives of TES addition included; stabilizing the Fe_3O_4 nanoparticles (Fe-NP), preventing the dissociation of Fe-NP from the biochar and increasing the quantity of N-containing functional groups for enhanced adsorption of metal ions. TES can be attached to the porous structure of biochar either through impregnation using weak Van Der Waals force [27] or grafting using strong covalent bonds to the biochar's functional groups. Partial impregnation of TES on the magnetic biochar during the functionalization stabilizes the Fe-NP on the surface improving the reusability of the adsorbent. Theoretically, surface functionalization with TES should afford a homogeneous coupling between surface OH groups and silanols from hydrolyzed TES [25, 26]. However, hydrogen bonding between surface OH and silanols/amino groups may also happen (Figure 1).

The amine functional groups of TES often increases the adsorption capacity due to complexation with heavy metals [7] [28]. Cu(II), Ni(II) and Pb(II) strongly bind to amine groups. Weaker binds have been observed between amine-containing sites and Cd(II) or Zn(II). However, they yet prefer amine sites to pure carboxylates. No preference has been observed for Ca(II) binding with amine compared with carboxylate ligand groups, indicating Ca(II) is bound by more negatively charged molecules [29]. Amine groups also effectively participate in the adsorption of Cr(VI). Amination with (3-aminopropyl) trimethoxysilane (APTMS), which is slightly lighter than TES, increased the Cr(VI) uptake of mesoporous silica from 36.95mg/g to 83.50mg/g [30]. Bamdad et al [25] applied two different chemical methods for amine functionalization of biochar, including i) nitration using concentrated nitric acid, followed by reduction, and (ii) condensation of aminopropyl triethoxysilane (TES) on the surface. Though the authors concluded that a moderate thermal activation is needed after amination, TES-aminated biochar indicated a higher CO_2 adsorption capacity compared to nitration-reduction.

3.2 Physical Activation of Biochar

Table 1. Surface area and porosity of raw and magnetized biochars

ID	BET Surface Area (m^2/g)	*Using Harkins and Jura Equation*		t-plot Micropore Volume (cm^3/g)
		t-plot Micropore Area (m^2/g)	t-plot mesopore surface area (m^2/g)	
Raw BC	219.98	123.44	96.54	0.0458
US30	261.67	193.22	68.45	0.0575
US 0 BC:Fe-2:1 TES5	190.88	112.23	78.65	0.0504
US30 BC:Fe-2:1 TES5	197.1	138.67	58.43	0.0563
US60 BC:Fe-2:1 TES5	214.86	155.43	59.43	0.0533
US30 BC:Fe-1:1 TES5	182.15	118.71	63.44	0.0349
US30 BC:Fe-2:1 TES5	197.1	138.67	58.43	0.0563
US30 BC:Fe-3:1 TES5	200.93	118.44	82.49	0.0525
US30 BC:Fe-2:1 TES5	197.1	138.67	58.43	0.0563
US30 BC:Fe-2:1 TES10	201.45	148.76	52.69	0.0379
US30 BC:Fe-2:1 TES15	181.65	125.98	55.67	0.0335

Table 1 shows the surface area, and total pore volume of raw, ultrasound activated and magnetized/functionalized biochars using different loadings of Fe-NP and TES concentrations. The specific surface area of BCs was calculated using the BrunauereEmmetteTeller (BET) and Harkins and Jura Equations. The impact of ultrasound activation on increasing the micro-porosity and surface area of BC has recently been proved as an effective method for the physical activation of biochar. This effect mainly attributes to the ultrasound-induced cavitation and its implications. Besides, the explosion of cavitation bubbles and generation of micro-jets can create a regular pattern of new pores into/onto the biochar surface which is visible in SEM images (Fig 2b vs Fig 2a). As a result, the BET surface area of raw biochar increased from 219.98 to 261.67 m^2/g after only 30 sec of BC exposure to ultrasound irradiation. On the other hand, the mesopore surface area reduced from 96.54 to 68.45 m^2/g due to their partial conversion to micropores. In other words, many macropores are broken down into micropores enhancing the overall surface with more porosities. As expected, the loading of nanoparticles and TES functionalization reduced micro and mesoporosity of biochar, which may cause a reduction in the adsorption capacity, yet exposure to 60sec of ultrasound activation could

sustain much of the BET surface area (214.86 m^2/g) compared with raw BC. Further porosity reduction was observed by increasing the concentration of TES or maximizing the loading of Nanoparticles. Accordingly, the minimum BET surface area of 182.15 and 181.65 m^2/g were observed for the samples containing either the maximum loading of Fe-NP (US30,BC:Fe-1:1,TES5) or TES (US30,BC:Fe-2:1,TES15).

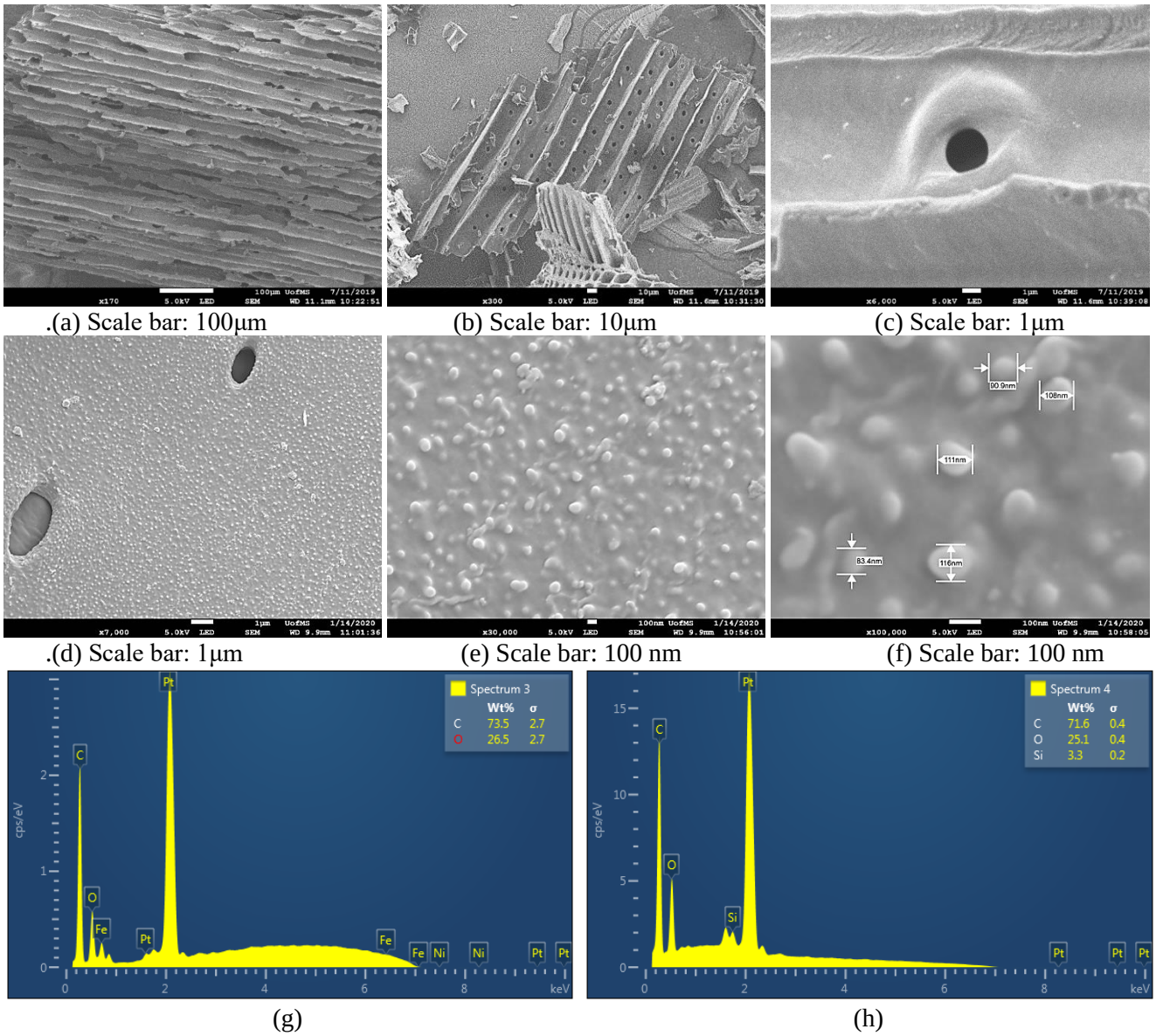

.(a) Scale bar: 100µm (b) Scale bar: 10µm (c) Scale bar: 1µm

.(d) Scale bar: 1µm (e) Scale bar: 100 nm (f) Scale bar: 100 nm

(g) (h)

Figure 2. SEM images of (a) raw biochar (longitudinal view), (b) ultrasound activated biochar, (c) ultrasound-generated pore with a diameter of 2 µm, (d, e, f) magnetized and functionalized surface. EDX analysis of (g) magnetized and (h) magnetized and functionalized biochar.

The SEM images also demonstrate the increased partial coating of biochar surface with TES and a uniform distribution of Fe-NP on BC surface (Fig 2 d-f). EDX analysis of the biochar surface (Figure 2 g-h) shows the elemental percentage composition of C, O, Fe and S in the magnetized and functionalized biochar where C content was found to be 71-73% and that of O and S is found to be 25-26% and 3.3 % respectively.

3.2.1 Effect of Physicochemical Magnetization on Elemental Composition of Biochar

Table 2. Elemental Analysis of raw and activated biochars

Sample	Carbon (% w/w)	Hydrogen (%w/w)	Nitrogen (%w/w)	Sulfur (%w/w)	Oxygen (%w/w)	Ash (%w/w)	Iron (% w/w)
Raw-BC	60.26	2.96	0.25	0.82	10.79	23.45	0.616
US 30-BC	66.56	2.32	0.21	0.61	9.93	21.20	0.438
US 0 ,BC:Fe 2:1,TES5	58.75	2.7	0.65	0.70	13.17	22.20	3.8
US 30,BC:Fe 2:1,TES5	54.65	2.24	0.51	0.62	12.59	21.42	7.98
US 60,BC:Fe 2:1,TES5	52.09	1.59	0.56	0.48	12.33	23.00	6.56
US 30,BC:Fe 1:1,TES5	57.42	2.18	0.75	0.87	12.92	22.60	7.33
US 30,BC:Fe 2:1,TES5	54.65	2.24	0.51	0.62	12.59	21.42	7.98
US 30,BC:Fe 3:1,TES5	54	2.07	0.49	0.52	12.31	24.52	9.01
US 30,BC:Fe 2:1,TES5	54.65	2.24	0.51	0.62	12.59	21.42	7.98
US 30,BC:Fe 2:1,TES10	57.6	2.09	0.70	0.47	12.21	23.40	8.62
US 30,BC:Fe 2:1,TES15	58.52	2.64	0.79	0.61	12.82	24.65	8.23

Table 2 lists the elemental (C, H, N, S, O and Fe) and ash contents of raw, ultrasound activated and magnetized biochars. As observed, the acoustic activation of biochar increases the C content of biochar, which is consistent with our previous works. Ultrasound cavitation and its implications (e.g. micro-jets, hot spots, shock waves, etc) can exfoliate the graphitic structure of biochar and facilitates the leaching of mineral compounds (ash content), which subsequently increase the portion of organic compounds in the biochar structure. In addition, the results suggested that acoustic activation reduces the oxygen content of biochar mainly through the removal of some of the oxygen-containing functional groups.

Upon magnetization and loading of Fe_3O_4 nanoparticles, the Fe and O contents of the samples increased as expected. Ultrasound activation also affects the loading of Fe_3O_4 Nanoparticles. As observed US0,BC:Fe 2:1,TES 5 contained the least Fe (3.8%) content. However, the Fe content increased to 7.93% and 6.56% for US30, BC:Fe 2:1,TES5 and US60,BC:Fe2:1,TES5, respectively. Compared to sonicated-functionalized BC, US0, BC:Fe 2:1,TES5 contained a higher quantity of C, H, and N. This may be due to higher porosity and surface area of the US-BC and subsequent incorporation of a higher quantity of Fe-NP into biochar structure which affects the % of other elements.

As expected, the increased ratio of BC to magnetic Nanoparticles reduced their loading and hence O contents declined. However, Fe content shows an increase, which is against our expectations. It should be explained that different combustion analyzers are used for the analysis of C, H, N, S; O; and Fe which needs different samples. This paradox between O and Fe trend can be due to the agglomeration of Nanoparticles in a sample. To get reasonable results and prevent such paradoxes, we synthesized three sets of samples and analyzed the elements three times. However, it was not possible to eliminate all the inaccuracies. The last section of the table focused on the effect of TES concentration during the process of functionalization. As observed N and ash contents significantly increased with TES concentration up to 10 ml/lit. However, a further increase of TES to 15 ml/lit just slightly increased the quantities of N and ash. As a result, the maximum N content was observed for US 30, BC:Fe 2:1,TES15.

3.2.2 Effect of Physiochemical Magnetization on Functional Groups of Biochar

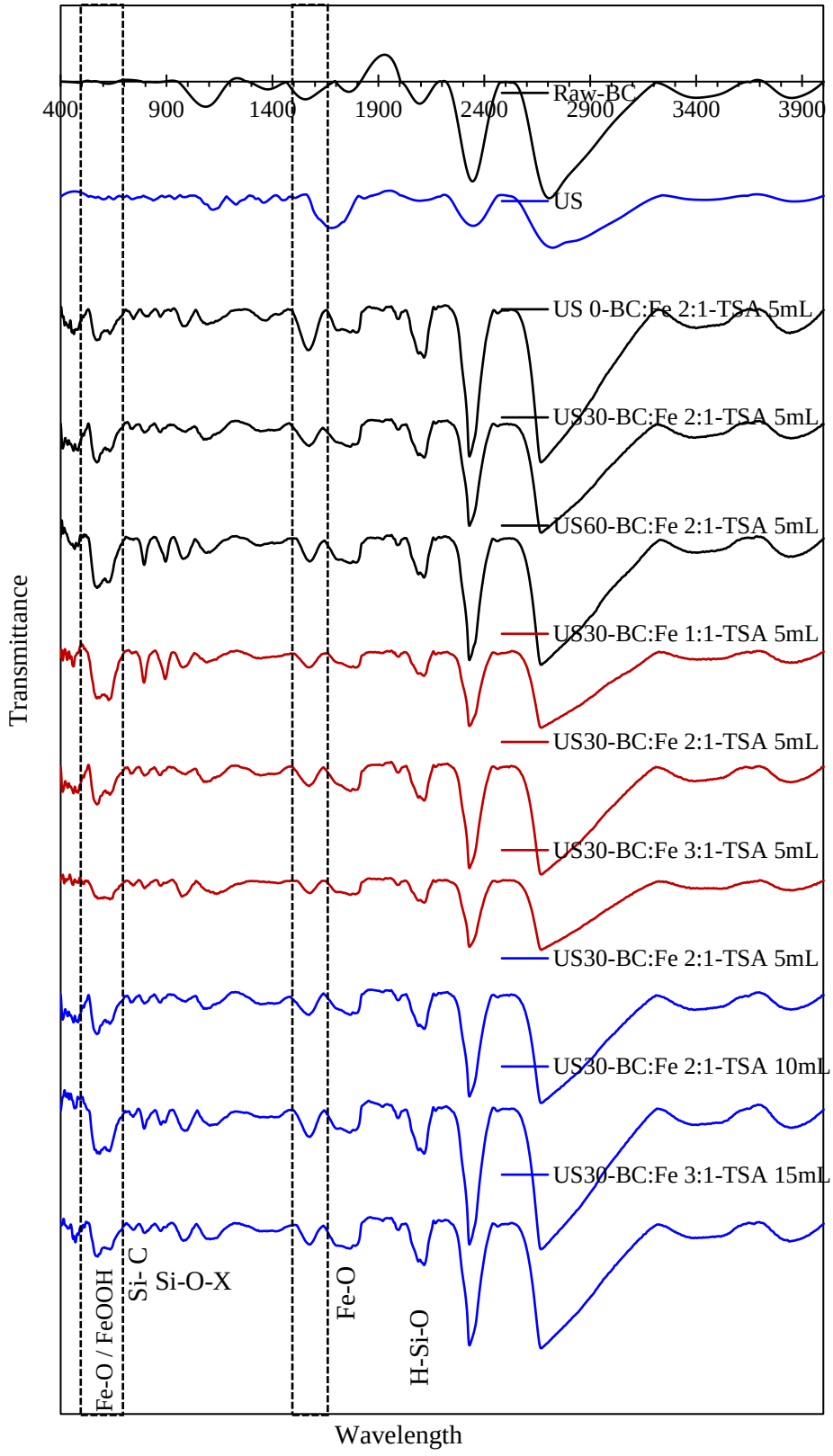

Figure 3. The effect of ultrasound irradiation on FTIR spectra of raw and the magnetized biochar. The effect of biochar to Fe nanoparticles ratio The effect of TES (3-(Triethoxysilyl)propylamine) concentration

The effects of magnetization and TES functionalization on functional groups of ultrasound-magnetite biochar under different conditions are provided in Figure 3. Data were analyzed by Origin software (Original data graphs in Appendix A.3.). The wide band at 3300-3600 cm^{-1} represents the stretching vibration of the hydrogen-bonded hydroxyl group. The intensification of this bond was significantly reduced due to ultrasound activation. This is consistent with our elemental analysis which confirms the reduction of O and H containing groups and our previous studies. According to the literature, the most prominent features of TES are located between 740-1250 cm^{-1} [31], [32], [33]. Accordingly, the characteristic peak at 765-795 cm^{-1} corresponds to the Si-C vibration [33], [34] or SiO-C [35], suggested that the organic alkyl chains are covalently bonded to the Si-O-Si networks [34], [36]. The other two peaks at and 952 cm^{-1} and 1047 cm^{-1} were assigned to the Si-O-C bond [33], [37], [35] and Si-O-Si stretching [34], [37], [35], respectively (herein referred to as the Si-O-X region). These two peaks can confirm the coating of the magnetite surface through the silanization reaction. The silica network is adsorbed on the surface by Si-O-C bonds [35], [38].

The peak at 1100 cm^{-1} is associated with either the stretching vibration of C-N of the incorporated C-NH_2 bond [33] or Si-O-C bond [39]. The observed Si-corresponded bands proved that TES was successfully grafted onto the magnetized biochar. The other new peak exhibited at 1580-1620 cm^{-1} was also assigned to the N-H bending of the NH_2 amine group [46,47], [39]. [35]. Additionally, the peak appeared at around 2200 which could be corresponded to H-Si-O [39]. There could be some overlap between the peaks. As an instance, a peak that is observed 1047 cm^{-1} could also be associated with Si-O-Fe stretching vibrations [36]. In addition, the two peaks valued at 1635 and 575 cm^{-1} are assigned to symmetrical and anti-symmetrical of the Fe–O vibrations [36, 40, 41] and a small peak next to it (at around 665 cm^{-1}) can result from the FeOOH stretching vibration, which

is usually appeared at the activated carbon modified by Fe^{3+} [42, 43]. It may also have some overlap with O-Si-O asymmetric flexing [44]. The presence of these two strong bonds in all magnetized samples suggested the attachment of magnetic nanoparticles to the biochar.

Upon magnetization and functionalization, the intensity of Fe-O (at 575 cm^{-1}) and Si-O-X (700-1200 peaks cm^{-1}) significantly increased. The highest intensities of Si-O-X and Fe-O (at 575 cm^{-1}) peaks were observed for the highest durations of ultrasound activation.

The FTIR spectra of magnetization using different loading of Fe_3O_4 nanoparticles are represented in maroon color in Figure 3. As expected the highest Fe-O peak (at 575 cm^{-1}) was observed for US30-BC:Fe 1:1-TES, since an equal quantity of biochar and Fe nanoparticles were used in the activation process. The intensity of this peak gradually decreased with the reduction of F-NP loading. Another important observation is that not only Fe-O peak but also the intensity of Si-O-X peaks are also significantly higher in US30-BC:Fe 1:1-TES sample, which can be due to the increased attachment of TES into this sample. However, it does not necessarily improve the adsorption capacity of biochar as this capability is a resultant of a series of phenomena including physical adoption, surface complexation, inner-sphere complexation, etc. Higher Fe and TES loading reduces the surface area and porosity of biochar which may negatively affect its adsorption capacity.

The lines highlighted in the blue color of Figure 3 demonstrate the effect of different TES concentrations in the amination step. The intensity of FTIR peaks of Si-O-X and Fe-O cm^{-1} increased with TES concentration up to 10 ml, however, no further increase in the intensity of peaks was observed with for higher concentration of TES up to 15, which is consistent with the trend of Fe and N contents in the samples.

3.2.3 Effect of Physiochemical Magnetization on graphitic structure of Biochar

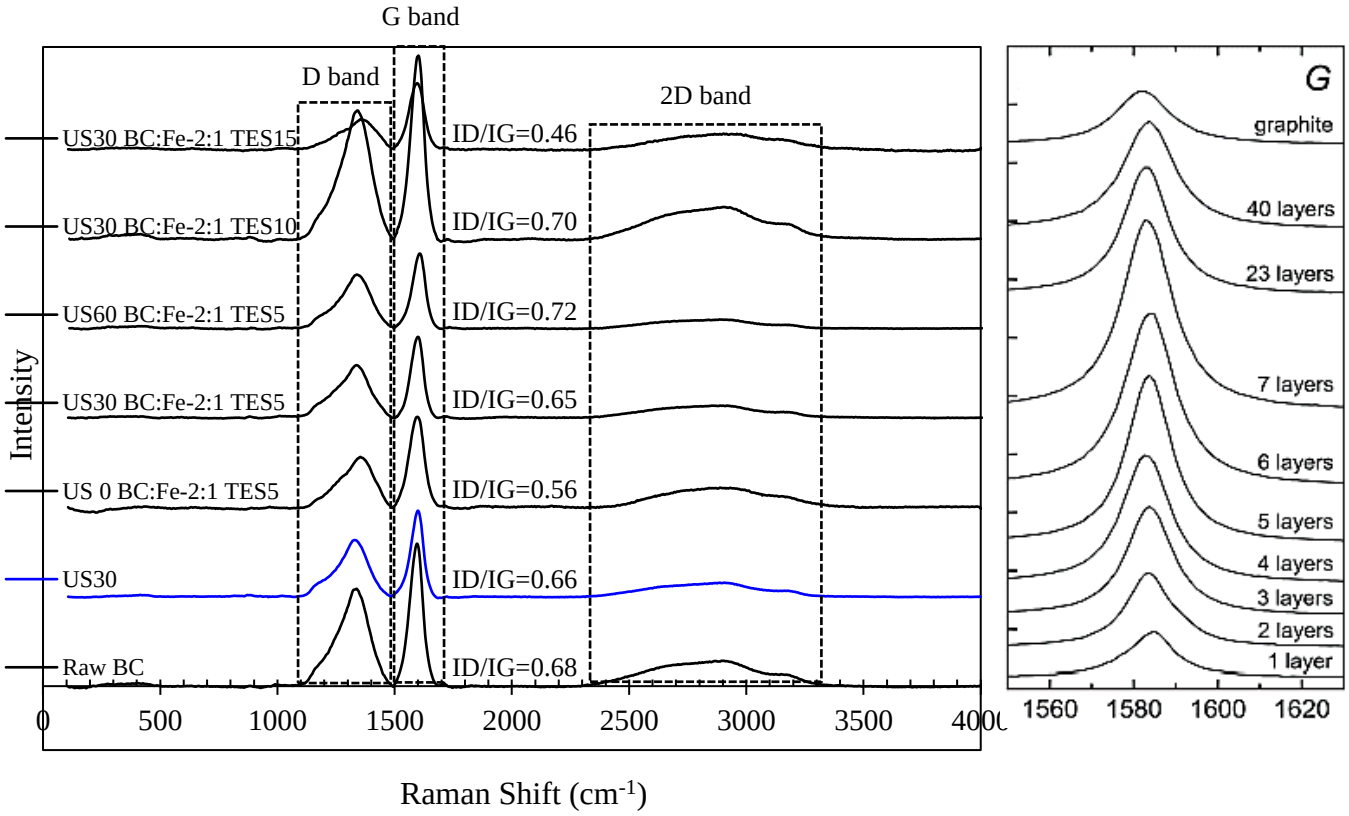

Figure 4. Raman Spectra of the biochars activated and functionalized under different ultrasound irradiation and TES loading (Left). Evolutions of the G band in the Raman spectrum as functions of the number of graphene layers, Reproduced (Right) [45].

Figure 4. shows the Raman Spectra of the biochar activated and functionalized under different ultrasound irradiation and TES loading. The spectra were recorded with a linear laser excitation of 532 nm and the baselines were revised. In general, their spectra share common features at around 1000-1529, 1500-1775, 2800 cm^{-1}, the so-called D, G, and 2D peaks respectively. The D-band (or "disorder-induced" peak) attributes to in-plane vibrations of sp^2-bonded carbon within structural defects, amorphous or disordered graphite. The D band has a low intensity in well-organized carbonaceous materials and graphite. However, it becomes equivalent to the G band for more disordered carbons such as biochar. The G-band (Stretching carbon-carbon sp^2 bonds) arises from the in-plane vibrations of the sp^2-bonded carbon in graphitic crystallites. The intensity ratio between

the D and G band (I_D/I_G) is a measure of defects in graphite-based materials. The comparable intensity of D-band and G-band with an intensity ratio ranging from 0.46 to 0.72 indicates that biochar is made of a high quantity of ordered and disordered graphitic carbons.

The 2D-band (also known as G′-band) is the second-order of the D-band and is the result of a two phonon lattice vibrational process, but unlike the D-band, it does not need to be activated by proximity to a defect. The 2D band is usually used to determine graphene layer thickness. It is much sharper and more intense in the single-layer graphene as in multi-layer graphene. According to the Raman results and as expected, the biochar structure involves multi-layer graphene mainly (graphitic structure).

It has been reported that the intensity of the G band increases with the number of graphene layers (for thin samples, up to 7 layers) and then decreases with the further increase of the number of layers (∼23, ∼40 layers and graphite) [45]. Raw chars usually contain clusters of 4 to 6 parallel graphene and graphitic oxide sheets [46, 47]. Therefore, reduced intensity of G peak can also be related to the exfoliation and reduction of biochar layers due to ultrasound activation. In addition, a lower intensity of D and G bands in ultrasound-activated samples can also indicate the size of crystallites reduces. This is consistent with our observation confirming the reduced biochar's particle size upon ultrasound activation.

The intensity of D and G peaks further reduced as a result of magnetization and functionalization. This indicates increasing the roughness and thickness of crystals due to the partial coating of the surface. However, the intensity of the D/G peak intensity ratio increases with ultrasound activation duration from 0.56 for US0-BS:Fe-2:1 TES5 to 0.72 for US60-BS:Fe-2:1 TES5. Generally, the maximum ID/IG ratios were observed in the samples activated with the highest ultrasound duration

(US60-BS:Fe-2:1 TES10)) and the TES concentration of 10ml/lit (US30-BS:Fe-2:1 TES10), indicating the increased defects or functional groups in the graphitic structure of these samples.

3.3 Heavy Metal Adsorption Studies

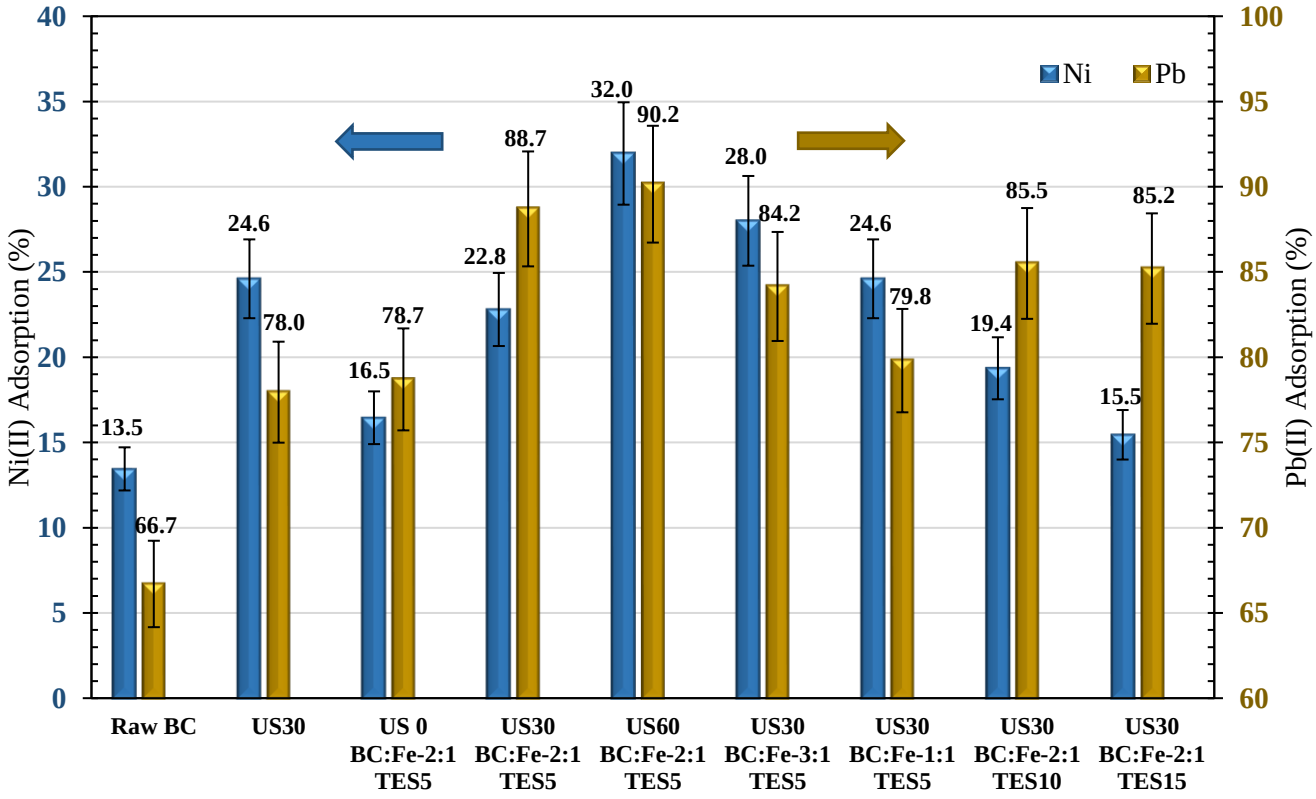

Figure 5. The effect of ultrasound activation, magnetization and TES functionalization on adsorption of Ni^{2+} and Pb^{2+} by biochar within 6 hours.

Acoustic Activation Effect: Figure 5 presents the performances of raw, activated, and magnetized biochars in adsorption of nickel and lead ions. All tests were repeated two times. As observed, raw biochar can remove only 14% of nickel and 67% of lead ions. Generally, the removal of Pb^{2+} ions in aqueous solution is easier than Ni^{2+} ions [48] (Page 60). The ionic radius, electronegativity (covalent bond strength) and the hydration properties of the metal ions are the principal properties used in the interpretation of heavy metal adsorption mechanisms. Structures with smaller hydrated

radius and higher electronegativity are more potential for surface complexation or adsorption reactions [49]. The degree of hydration of metal ions depends on the ratio of charge (electrostatic charge) to volume. A lower number of water molecules hydrate the greater ions with smaller charges per volume. Pb(II) ions have a larger ionic radius than Ni(II) ions (0.119 vs 0.069nm); however, the hydrated radius of Pb(II) ions is smaller than that of Ni(II) ions (0.401nm vs 0.404 nm) [50]. Larger ionic radius and hence smaller hydrated one should be adsorbed more strongly. On the other hand, the stronger covalent bonds should be formed with more electronegative metals. The combination of higher electronegativity and a smaller hydration radius ensures a higher covalent bond between the metal ion and the electron donor of the adsorbent surface [48] (Page 60), [51].

Short term physical activation of biochar with ultrasound irradiation could increase the nickel removal to 25% and lead removal to 78%. This improvement was caused by the ultrasound cavitation and its implications which subsequently increased the surface area and porosity of BC. Additionally, micro-jets can generate new pores and open some of the blocked pores which not only increases the porosity of biochar but also make channels to the under-layers of biochar where some functional groups are trapped. These effects favor both magnetization and functionalization steps as well.

Magnetization usually decreases the adsorption capacity of biochar. However, comparing the adsorption results of US0-BC:Fe2:1-TES5 demonstrated the contribution of amine functionalization which not only prevented the reduction of metal removal but also slightly increased of adsorption capacity of biochar compared to raw biochar. Acoustic activation of biochar prior to magnetization and functionalization significantly increased the metal removal compared with raw biochar. Given the fact that the maximum nickel and lead removal is 17% and 79 % for US0-BC:Fe 2:1-TES5, further increase of Ni and Pb adsorption (32% and 90% respectively) attributes to the structural modification using ultrasound irradiation.

Magnetization effect: Magnetization process was conducted using three different BC: Fe ratios of 1:1, 2:1, and 3:1. Generally, the lower the nanoparticle loading, the greater the adsorption capacity. The reduction of biochar's adsorption capacity with nanoparticle loading is mainly due to their role in reducing the surface area and the porosity of biochar. Therefore, among the three Fe_3O_4 loadings with 30 sec of acoustic pre-activation, the maximum Ni(II) adsorption of 28% were observed for US30-BC:Fe 3:1-TES5 which contained the lowest quantity of Fe_3O_4 nanoparticles. The value further increased to 32% for US60-BC:Fe 3:1-TES5. Moreover, longer acoustic activation significantly reduced the adsorption time (increased the adsorption rate, in other words). The highest amount of nickel was removed by US60-BC:Fe 3:1-TES5 only within 2 hours. In terms of lead removal, the highest absorption was observed by US30-BC:Fe 2:1-TES5. However, in this case, also the sample containing the highest Fe-NP indicated the least adsorption.

Functionalization effect: The highest adsorption of both Ni(II) and Pb(II), was observed for the sample containing the lowest TES loading, US30-BC:Fe2:1-TES5. Further increasing TES concentration reduced the adsorption capacity of the activated biochars. This can be due to the significant impact of chemical functionalization in reducing the surface area and porosity of adsorbent, particularly in terms of Ni(II) adsorption. However, the impact of TES in increasing the removal of Pb(II) can be noticed by comparing the results of US30 and US30BC:Fe 2:1 TES5. This observation suggests the more determinant role of chemisorption in Pb removal. Prominent capability of TES in removal of lead and other heavy metals has also been reported by other researchers [52]. Kong et al [53] functionalized the surface of silica nanoparticles by three silane coupling agents, such as (3-Mercaptopropyl) triethoxysilane (MPTES) and (3-Amincpropyl) trithoxysilane (TES) and compared their performances on the removal of Pb(II), Cu(II), Hg(II),

Cd(II), Zn(II). TES functionalized silica nanoparticles (SiO_2-TES) exhibited maximum removal efficiency towards Pb^{2+} and Hg^{2+}. Shi et al [54] also synthesized magnetic biochar in three steps, including preparation of carboxylated biochar, synthesis of Fe_3O_4@SiO_2-NH_2 particles from Fe_3O_4 particles by modified with TEOS and TES via "Stober" method and then conjugated the Fe_3O_4@SiO_2-NH_2 with carboxylated biochar by forming amide bond via the classic EDC-NHS coupling. The Cr(VI) ions adsorption capacity of magnetic biochar was 27.2 $mg \cdot g^{-1}$, surpassing original carboxylated biochar (18.2 $mg \cdot g^{-1}$). Compared to their work, the method developed in this study is much simpler. In addition, the focus of the current work is promoting the adsorption and functionalization capability of biochar rather than using it as a carrier or support. And the last priory of this study over the other similar works is that pH as a master variable in adsorption of heavy metals was not adjusted in this study and the adsorption was conducted on the inherent pH of the solution.

3.4 Kinetic and the Equilibrium Adsorption

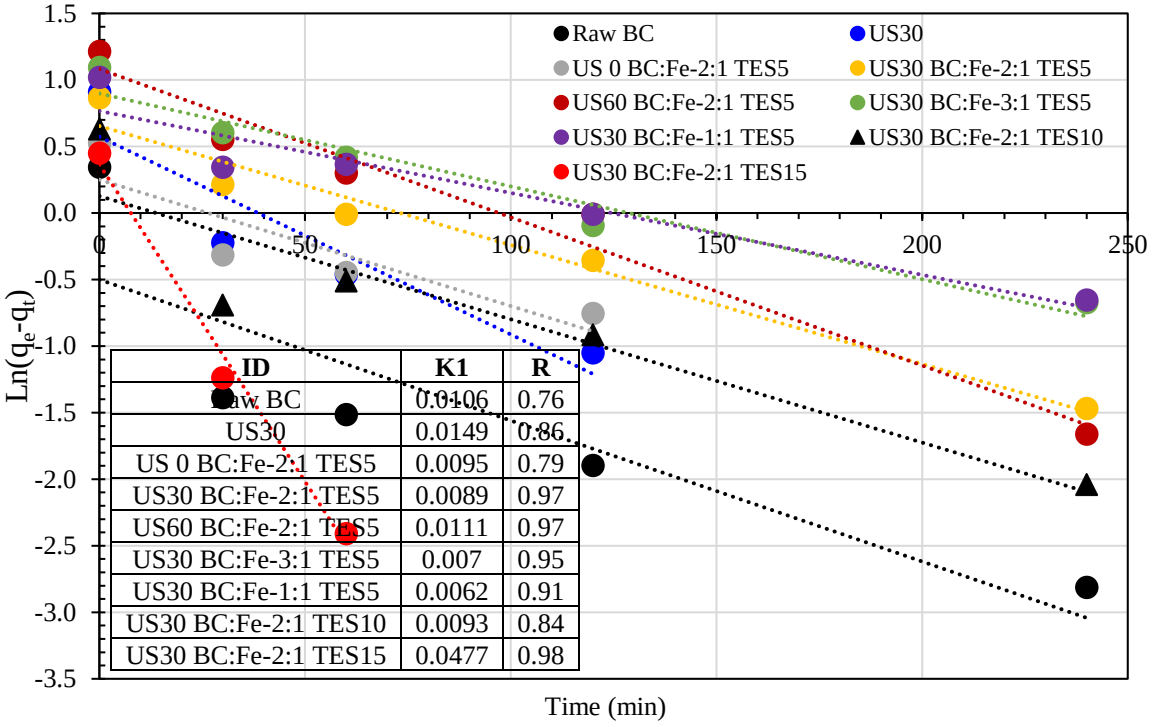

ID	K1	R
Raw BC	0.0106	0.76
US30	0.0149	0.86
US 0 BC:Fe-2:1 TES5	0.0095	0.79
US30 BC:Fe-2:1 TES5	0.0089	0.97
US60 BC:Fe-2:1 TES5	0.0111	0.97
US30 BC:Fe-3:1 TES5	0.007	0.95
US30 BC:Fe-1:1 TES5	0.0062	0.91
US30 BC:Fe-2:1 TES10	0.0093	0.84
US30 BC:Fe-2:1 TES15	0.0477	0.98

(a)

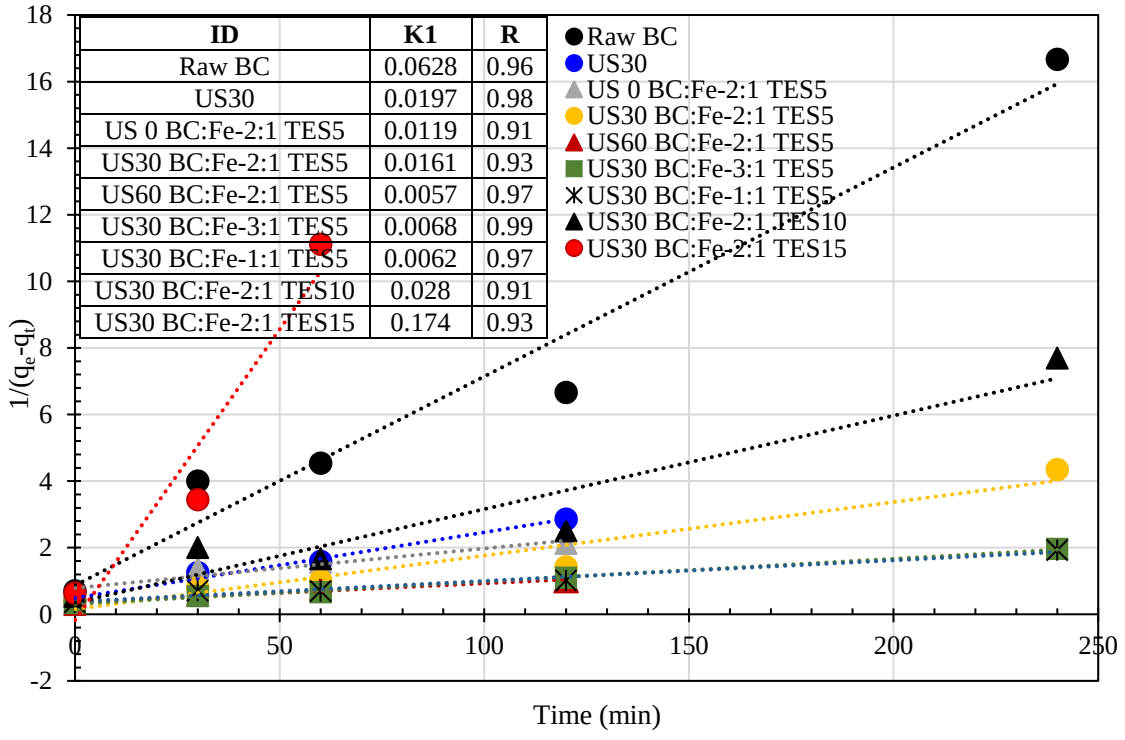

ID	K1	R
Raw BC	0.0628	0.96
US30	0.0197	0.98
US 0 BC:Fe-2:1 TES5	0.0119	0.91
US30 BC:Fe-2:1 TES5	0.0161	0.93
US60 BC:Fe-2:1 TES5	0.0057	0.97
US30 BC:Fe-3:1 TES5	0.0068	0.99
US30 BC:Fe-1:1 TES5	0.0062	0.97
US30 BC:Fe-2:1 TES10	0.028	0.91
US30 BC:Fe-2:1 TES15	0.174	0.93

(b)

Figure 6 (a) Pseudo-first-order and (b) pseudo-second-order models for Ni (II) adsorption onto Raw Ultrasound activated, magnetized/functionalized biochars. (C_0[Ni(II)]= 100 mg L^{-1}, V=50 ml, M= 50 mg)

The equilibrium adsorption capacities for Ni(II) and Pb(II) was calculated according to $q_e = \frac{(C_0 - C_e)V}{M}$, where C_0, C_e, V and M are the initial and the residual concentration of metal ions in the solution ($mg.L^{-1}$), the volume of heavy metal solution (mL) and the amount of adsorbents (mg), respectively. In addition, the pseudo-first-order ($\ln(q_e - q_t) = lnq_e - k_1 t$)and pseudo-second-order $\left(\frac{t}{q_t} = \frac{1}{k_2 q_e^2} + \frac{1}{q_e} t\right)$equations were used to model the adsorption process. Based on the analysis presented in Figure 6, the pseudo-second-order model was more suitable for explaining the behavior of Pb adsorption into magnetized biochar, indicating that the reaction is more inclined towards chemisorption due to the impact of functional groups on biochar surface rather than physisorption. However, in terms of Ni (II), both pseudo-first-order also show reasonable R values, suggesting the prominent impact of both physisorption and chemisorption in Ni removal.

4 Conclusion

Traditional magnetization through impregnation, co-precipitation, and liquid reduction has several major disadvantages, on top of that is the reduction of biochar's adsorption capacity. This study introduced a post-pyrolysis acoustic-based magnetization process which not only prevented the reduction of biochar adsorption capacity but also further improved it. The process includes three subsequent steps, including acoustic modification of biochar's structure followed by loading of Fe_3O_4 nanoparticles and functionalization using 3-(triethoxysilyl)propylamine (TES). In addition to immobilization of nanoparticles, TES functionalization increased the N-containing functional groups which further improved the adsorption capacity of biochar. The physical and chemical properties of magnetic biochar were characterized by Fourier-Transform Infrared Spectroscopy (FTIR), Raman spectroscopy, combustion analysis (organic contents), Scanning electron microscope, Transmission electron microscopy, and Sorptoanalysis. The synthesized biochar was

further tested for removal of lead and nickel, which demonstrated significant higher metal removal within a shorter duration. While raw biochar could remove only 13% and 68% of Ni and Pb with some signs of leaching, the biochar activated under 60 sec of ultrasound irradiation, magnetized with Fe3O4 with the ratio of 2:1 and functionalized with the least concentration of TES exhibited 32% and 90% of Ni and Pb removal without any leaching. In addition, magnetized biochar could further reduce the adsorption duration of nickel and lead from 8 to 2 hours and 1 hour respectively.

5 Acknowledgements

The author is grateful for the financial support of the National Science Foundation (NSF EPSCoR RII Grant No. OIA-1632899) of the United States. The author also appreciates the UM Science, Technology, Engineering, and Math Summer Research Experience for Undergraduates (STEMS REU) Program at the University of Mississippi. Financial Support from the Sally McDonnell Barksdale Honors College is also greatly appreciated.

References

1. Barakat, M.A., *New trends in removing heavy metals from industrial wastewater.* Arabian Journal of Chemistry, 2011. **4**(4): p. 361-377.
2. Cobbina, S., et al., *Comparative Assessment of Heavy Metals in Drinking Water Sources in Two Small-Scale Mining Communities in Northern Ghana*. Vol. 12. 2015. 10620-10634.
3. Babel, S. and T.A. Kurniawan, *Cr(VI) removal from synthetic wastewater using coconut shell charcoal and commercial activated carbon modified with oxidizing agents and/or chitosan.* Chemosphere, 2004. **54**(7): p. 951-967.
4. Li, H., et al., *Mechanisms of metal sorption by biochars: Biochar characteristics and modifications.* Chemosphere, 2017. **178**: p. 466-478.
5. Mohan, D., et al., *Sorption of arsenic, cadmium, and lead by chars produced from fast pyrolysis of wood and bark during bio-oil production.* Journal of Colloid and Interface Science, 2007. **310**(1): p. 57-73.
6. Mohan, D., et al., *Organic and inorganic contaminants removal from water with biochar, a renewable, low cost and sustainable adsorbent – A critical review.* Bioresource Technology, 2014. **160**: p. 191-202.
7. Lu, H., et al., *Relative distribution of Pb2+ sorption mechanisms by sludge-derived biochar.* Water Research, 2012. **46**(3): p. 854-862.
8. Karunanayake, A.G., et al., *Lead and cadmium remediation using magnetized and nonmagnetized biochar from Douglas fir.* Chemical Engineering Journal, 2018. **331**: p. 480-491.
9. Mian, M.M., et al., *Simultaneous functionalization and magnetization of biochar via NH3 ambiance pyrolysis for efficient removal of Cr (VI).* Chemosphere, 2018. **208**: p. 712-721.
10. Chen, B., Z. Chen, and S. Lv, *A novel magnetic biochar efficiently sorbs organic pollutants and phosphate.* Bioresource Technology, 2011. **102**(2): p. 716-723.
11. Zhou, Z., et al., *Sorption performance and mechanisms of arsenic(V) removal by magnetic gelatin-modified biochar.* Chemical Engineering Journal, 2017. **314**: p. 223-231.
12. Thines, K.R., et al., *Synthesis of magnetic biochar from agricultural waste biomass to enhancing route for waste water and polymer application: A review.* Renewable and Sustainable Energy Reviews, 2017. **67**: p. 257-276.
13. Zhang, M., et al., *Preparation and characterization of a novel magnetic biochar for arsenic removal.* Bioresource Technology, 2013. **130**: p. 457-462.
14. Mohan, D., et al., *Lead sorptive removal using magnetic and nonmagnetic fast pyrolysis energy cane biochars.* Journal of Colloid and Interface Science, 2015. **448**: p. 238-250.
15. Gazi, M., A. Oladipo, and K. Azalok, *Highly efficient and magnetically separable palm seed-based biochar for the removal of nickel*. 2018.
16. Zhao, Y., et al., *Green preparation of magnetic biochar for the effective accumulation of Pb(II): Performance and mechanism.* Chemical Engineering Journal, 2019. **375**: p. 122011.
17. Suslick, K.S., D.A. Hammerton, and R.E. Cline, *Sonochemical hot spot.* Journal of the American Chemical Society, 1986. **108**(18): p. 5641-5642.
18. Suslick, K.S., *Sonochemistry.* Science, 1990. **247**(4949): p. 1439.
19. Sanderson, B., *Applied sonochemistry – the uses of power ultrasound in chemistry and processing. By Timothy J Mason and John P Lorimer, Wiley-VCH Verlag, Weinheim, 2002, 303 pp, ISBN 3-527-30205-0.* Journal of Chemical Technology & Biotechnology, 2004. **79**(2): p. 207-208.
20. Stankovich, S., et al., *Graphene-based composite materials.* Nature, 2006. **442**(7100): p. 282-286.
21. Chatterjee, R., et al., *Ultrasound cavitation intensified amine functionalization: A feasible strategy for enhancing CO2 capture capacity of biochar.* Fuel, 2018. **225**: p. 287-298.
22. Wu, X., H. Zhao, and J. Pei, *Fabrication of nanopore in graphene by electron and ion beam irradiation: Influence of graphene thickness and substrate.* Computational Materials Science, 2015. **102**: p. 258-266.
23. Sajjadi, B., et al., *Variables governing the initial stages of the synergisms of ultrasonic treatment of biochar in water with dissolved CO_2.* Fuel, 2019. **235**: p. 1131-1145.

24. Chen, W.-Y., et al., *Photochemical and acoustic interactions of biochar with CO2 and H2O: Applications in power generation and CO2 capture.* AIChE Journal, 2014. **60**(3): p. 1054-1065.
25. Bamdad, H., K. Hawboldt, and S. MacQuarrie, *Nitrogen Functionalized Biochar as a Renewable Adsorbent for Efficient CO2 Removal.* Energy & Fuels, 2018. **32**(11): p. 11742-11748.
26. Russo, L., et al., *Carbonate hydroxyapatite functionalization: a comparative study towards (bio)molecules fixation.* Interface Focus, 2014. **4**(1): p. 20130040.
27. Houshmand, A., W.M.A. Wan Daud, and M.S. Shafeeyan, *Exploring Potential Methods for Anchoring Amine Groups on the Surface of Activated Carbon for CO_2 Adsorption.* Separation Science and Technology, 2011. **46**(7): p. 1098-1112.
28. Chen, D., et al., *Functionalization of 4-aminothiophenol and 3-aminopropyltriethoxysilane with graphene oxide for potential dye and copper removal.* Journal of Hazardous Materials, 2016. **310**: p. 179-187.
29. Cabaniss, S.E., *Forward Modeling of Metal Complexation by NOM: II. Prediction of Binding Site Properties.* Environmental Science & Technology, 2011. **45**(8): p. 3202-3209.
30. Kim, S.-S., et al., *Strain-Assisted Wafer-Scale Nanoperforation of Single-Layer Graphene by Arrayed Pt Nanoparticles.* Chemistry of Materials, 2015. **27**(20): p. 7003-7010.
31. Zhou, T., et al., *Efficient capture of aqueous humic acid using a functionalized stereoscopic porous activated carbon based on poly(acrylic acid)/food-waste hydrogel.* Journal of Environmental Sciences, 2019. **77**: p. 104-114.
32. Balakrishnan, S.R., et al., *Polysilicon nanogap lab-on-chip facilitates multiplex analyses with single analyte*. Biosens Bioelectron, 2016. **84**: p. 44-52.
33. Ling, P.A. and H. Ismail, *Tensile Properties, Water Uptake, and Thermal Properties of Polypropylene/Waste Pulverized Tire/Kenaf (PP/WPT/KNF) Composites*. 2012. Vol. 8. 2012.
34. Cui, F. and T. Cui, *Self-catalytic synthesis of metal oxide nanoclusters@mesoporous silica composites based on successive spontaneous reactions at near neutral conditions.* Chemical Communications, 2014. **50**(94): p. 14801-14804.
35. Vieillard, J., et al., *Cocoa shell-deriving hydrochar modified through aminosilane grafting and cobalt particle dispersion as potential carbon dioxide adsorbent.* Chemical Engineering Journal, 2018. **342**: p. 420-428.
36. Shi, S., et al., *Enhanced Cr(VI) removal from acidic solutions using biochar modified by Fe3O4@SiO2-NH2 particles.* Science of The Total Environment, 2018. **628-629**: p. 499-508.
37. Pasternack, R.M., S. Rivillon Amy, and Y.J. Chabal, *Attachment of 3-(Aminopropyl)triethoxysilane on Silicon Oxide Surfaces: Dependence on Solution Temperature.* Langmuir, 2008. **24**(22): p. 12963-12971.
38. Salili, S.M., et al., *Characterization of mechano-thermally synthesized Curie temperature-adjusted La0.8Sr0.2MnO3 nanoparticles coated with (3-aminopropyl) triethoxysilane.* Materials Characterization, 2015. **106**: p. 78-85.
39. Majoul, N., S. Aouida, and B. Bessaïs, *Progress of porous silicon APTES-functionalization by FTIR investigations.* Applied Surface Science, 2015. **331**: p. 388-391.
40. Lim, J.Y., et al., *Novel fabrication of functionalized graphene oxide via magnetite and 1-butyl-3-methylimidazolium tetrafluoroborate.* Nano-Structures & Nano-Objects, 2018. **16**: p. 403-411.
41. Wei, W., et al., *Controllable synthesis of magnetic Fe3O4 encapsulated semimetal Bi nanospheres with excellent stability and catalytic activity.* Journal of Materials Science, 2018. **53**(19): p. 13886-13899.
42. Liu, Y., et al., *Efficient Adsorption of Sulfamethazine onto Modified Activated Carbon: A Plausible Adsorption Mechanism.* Scientific Reports, 2017. **7**(1): p. 12437.
43. Pham, X.N., et al., *Synthesis and characterization of chitosan-coated magnetite nanoparticles and their application in curcumin drug delivery.* Advances in Natural Sciences: Nanoscience and Nanotechnology, 2016. **7**(4): p. 045010.

44. Huang, Z., et al., *Efficient Removal of Co2+ from Aqueous Solution by 3-Aminopropyltriethoxysilane Functionalized Montmorillonite with Enhanced Adsorption Capacity.* PLOS ONE, 2016. **11**(7): p. e0159802.
45. Yoon, D., et al., *Variations in the Raman Spectrum as a Function of the Number of Graphene Layers.* Journal of the Korean Physical Society, 2008. **55**(3): p. 1299-1303.
46. Franklin, R.E., *Crystallite growth in graphitizing and non-graphitizing carbons.* Proceedings of the Royal Society of London. Series A. Mathematical and Physical Sciences, 1951. **209**(1097): p. 196-218.
47. Hammes K and Schmidt MWI, eds. *Changes of biochar in soil. in: Lehmann J., Joseph S. (ed.), Biochar for environmental management, science and technolog*. 2009: United Kingdom: EarthScan.
48. HOLMBERG, J.P., *Competitive Adsorption and Displacement Behaviour of Heavy Metals on Peat* in *Department of Civil and Environmental Engineering* 2006, Chalmers University of Technology.
49. Zhan, W., et al., *Adsorption of Cu(ii), Zn(ii), and Pb(ii) from aqueous single and binary metal solutions by regenerated cellulose and sodium alginate chemically modified with polyethyleneimine.* RSC Advances, 2018. **8**(33): p. 18723-18733.
50. Nightingale, E.R., *Phenomenological Theory of Ion Solvation. Effective Radii of Hydrated Ions.* The Journal of Physical Chemistry, 1959. **63**(9): p. 1381-1387.
51. Puranik, P.R. and K.M. Paknikar, *Influence of co-cations on biosorption of lead and zinc – a comparative evaluation in binary and multimetal systems.* Bioresource Technology, 1999. **70**(3): p. 269-276.
52. Tang, S., et al., *Amino-functionalized sewage sludge-derived biochar as sustainable efficient adsorbent for Cu(II) removal.* Waste Management, 2019. **90**: p. 17-28.
53. Kong, X.-f., et al., *Selective removal of heavy metal ions from aqueous solutions with surface functionalized silica nanoparticles by different functional groups.* Journal of Central South University, 2014. **21**(9): p. 3575-3579.
54. Shi, S., et al., *Enhanced Cr(VI) removal from acidic solutions using biochar modified by Fe3O4@SiO2-NH2 particles.* Sci Total Environ, 2018. **628-629**: p. 499-508.

Appendix

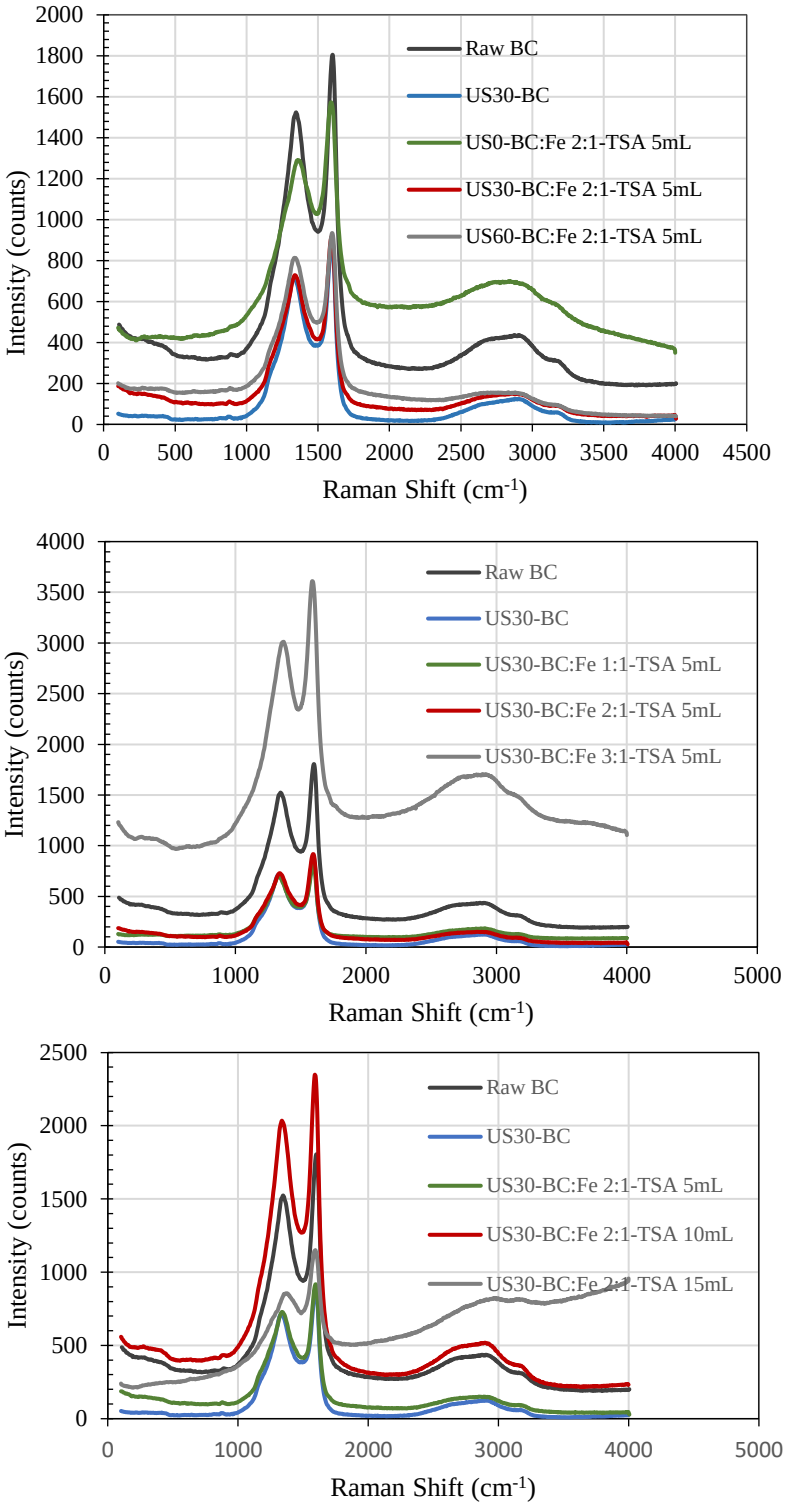

A.1. Raman plots of raw and magnetized biochar

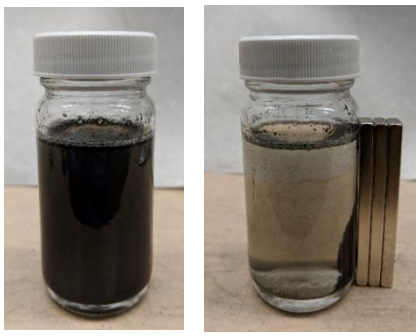

A.2. Separation of 0.5g Biochar in 50 mL water by neodymium magnet.

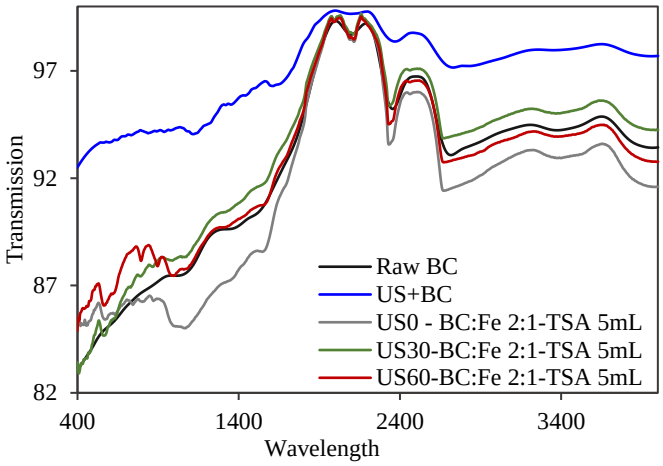

(a)

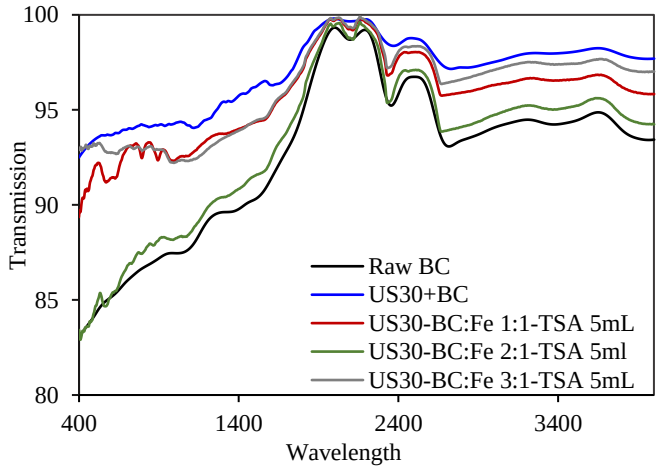

(b)

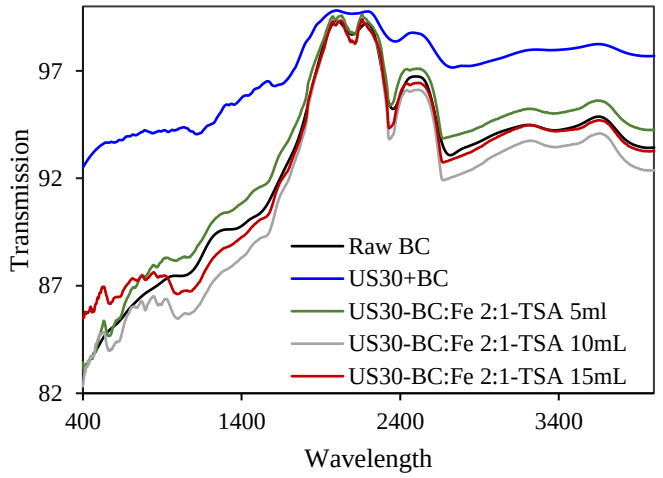

(c)

A.3. FTIR spectra of raw and the magnetized biochar. a) The effect of ultrasound irradiation b). The effect of biochar to Fe nanoparticles ratio, c) The effect of TES (3-(Triethoxysilyl)propylamine) concentration. The baselines of the graphs were revised in Origin lab (Version 2019b).

A.3. 2400 CHNS/O Series II System, Perkin Elmer (Anderson 222, University MS)

A.4. DR6000 UV VIS Spectrophotometer (Anderson 223, University MS)

A.5. JSM 7200 FLV Field Emission Scanning Electron Microscope (Thad Cochran Research Center, MS)

A.6. 3Flex Surface Characterization Analyzer, Micromeritics (Anderson 223, University MS)

A.7. Cary 660 FTIR Spectrometer (Coulter, University MS)